Cratering and spall simulation of Pokhran-1 event with three-dimensional transient finite element analysis

Rajeev Ranjan, R. K. Singh*, S. K. Sikka and Anil Kakodkar

Bhabha Atomic Research Centre, Trombay, Mumbai 400 085, India

Three-dimensional transient numerical simulation of coupled gas cavity and geological medium problem resulting from underground nuclear explosion events is complex due to the gas cavity growth, resulting into the large deformations and large strains of the geological medium and shock-induced high strain-rate dependence of the response. However, it is important to establish the effects of local inelastic and nonlinear behaviour due to crushing and cracking of the geological medium, on the shock-waves near the source and the seismic signals beyond the elastic radius. This study also helps simulate the shock-wave reflection effects from the free surface near the ground zero, mound growth, spall near the free surface and the subsequent free fall of the mound due to gravity effect resulting in crater formation. The impacting spalled rock layers give rise to secondary seismic signals in addition to the primary signals that are observed in the near field which in turn are known to influence the far-field seismic signals. The present article describes the capabilities of a three-dimensional transient finite element code, SHOCK-3D, for the short-time cavity growth, shock-wave propagation, mound growth and its free fall along with the settlement of the mound observed after a longer duration for the composite layer medium. The code predictions are benchmarked for the near-source experimental observations of the first Indian nuclear explosion event of 1974, carried out at the Pokhran test site.

THE present article describes a methodology that has been evolved with the three-dimensional finite element code, SHOCK-3D, for the numerical simulation of nuclear explosion events for short and long duration wave propagation in the composite layer medium. It is important to model the geological layers appropriately to pick up the shock-wave reflections from the layer interfaces due to different rock formations and the free surface at ground zero. These aspects have been suitably modelled for Pokhran-1974 nuclear explosion event and all the experimental observations reported by Chidambaram *et al.*[1,2]; namely cavity size, maximum mound velocity and maximum mound height have been computed with excellent accuracy. To analyse the problem for longer time duration, radiation boundary condition is applied at surfaces, which are beyond the elastic radius from the source to avoid any spurious reflections from the numerical model boundary. In addition, the influence of gravity is also simulated to estimate the impact or slap-down effects of the spalled rock layers on the close in-ground acceleration signals, which in turn influence the seismic signals.

The important inputs to analyse the problem are source strength, rock dynamics properties describing the constitutive equations and Hugoniot equation of state for different rock layers. A short time transient computation of 2.5 s duration for Pokhran-1974 event is carried out to study the resulting oblong cavity growth, chimney formation, and mound growth. Shock-wave reflections from the free surface and interfaces of shale, sandstone and top layer of degraded sandstone, and the resulting spall are adequately simulated in this study. Further, a long-time-transient computation of 20 s duration is carried out for the event to study the free fall of the mound, leading to crater formation after the settlement of the falling mound due to the gravity effect. The crack profile due to the explosion near the zero ground (GZ) is predicted and is found to be consistent with that observed in the post-shot examinations.

The vertical ground seismic acceleration recorded near the source at a distance of 135 m from the zero ground, as reported by Chidambaram *et al.*[1] is successfully simulated with the present computational synthetic signal. The close in ground synthetic acceleration signals are noted to be consistent with the observed acceleration signal at the test site. In addition, the initial peak acceleration value and the secondary acceleration peak value generated due to the spall-induced mound fall-back at the composite layer interface are truly represented by the numerical model. Finally, some observations are made about the effectiveness of SHOCK-3D code to predict the short-term and long-term transient response of underground nuclear events through the present numerical simulation.

Phenomenology of underground nuclear explosion and numerical simulation studies

The phenomenology of underground nuclear explosion event is quite complex and requires deep insight into shock-wave propagation, inelastic and elastic wave propagation and

*For correspondence. (e-mail: rksingh@magnum.barc.ernet.in)

behaviour of the different rock strata for successful numerical simulation studies. Excellent reviews of the underground nuclear explosion phenomenology have been presented[3,4]. A brief review of the phenomenology and numerical schemes for the simulation of underground nuclear explosion events is presented in this section.

After the release of energy from an underground nuclear explosion source, instantly, within a few microseconds, the device and the surrounding rocks are vaporized. The vapour expands radially outward and under the influence of high-pressure and heat (~a few millions of atmosphere pressure and millions of Kelvin temperature), a strong shock-wave is driven into the rock medium, which results into additional vaporization and melting of the rock medium and thus a large cavity is formed. The near-source effects include the growth of spherical cavity driven by the high-pressure gases up to a size such that the pressure within the cavity is finally balanced by the confining stresses due to the overburden. Subsequently, the cavity shrinks due to the elastic recovery and a residual compressive hoop stress field is generated near the cavity, which together with the overburden holds the cavity gases and is required for efficient containment. In addition, shock-wave propagation in the rock medium causes inelastic deformation and crushing of rock mass. After some distance from the source, the shock-waves become weak due to attenuation and energy dissipation. Propagation of inelastic stress waves is followed by subsequent propagation of elastic and anelastic waves, which generate seismic waves. In case of small depth of burial, initially the zero ground area develops into a dome-shaped mound and the ground is uplifted. Subsequently, with the reflection of the stress waves from the free surface; the tension waves are generated. At times, the reflected tension waves have sufficient energy to overcome the combined energy of the upcoming compression waves from the source, the tensile strength of the rock mass and the overburden. This phenomenon results into spall of rock mass near the subsurface region at zero ground. Location of the spall depends on the scaled depth of burial, tensile strength of the rock mass and the overburden stress, which are site-specific. The rock layers above the spall zone during the mound growth fall-back and impact the bottom rock layers, which is known as the spall closure or 'slap-down effect'. Other features are the formation of surface cracks and compaction of overlying strata. The reflected tension waves also alter the cavity shape from the initial spherical shape to an oblong shape, with major dimension of the cavity along the vertical direction. This again depends on the scaled depth of burial and rock properties, since for deeply buried sources, the cavity growth would be nearly spherical.

After a few seconds the cavity gases cool and condense with resulting fall in the cavity pressure. This may cause cavity-wall collapse and the overlying fractured rock layers are deposited as rubble; above the oblong cavity, a cylindrical collapse mechanism with a typical chimney-like structure is developed. The extent of chimney growth towards zero ground would depend on the rubble-filling capacity of the collapse regime, void size due to cavity collapse, strength of rock that can support the overburden and scaled depth of burial. In case of small scaled depth of burial, the chimney may grow up to zero ground and a collapse sink is formed. For shallow depth of burial, the interaction of collapse chimney with free surface and tensile rupture of top layers may result in the formation of a rubble mound. For an extremely shallow depth of burial, the resulting top layer failure may be extensive and the cavity may be exposed to the environment, which could result in venting. The efficient containment of such experiments depends on the design of emplacement cavity, the *in situ* rock mass properties and the overburden. At shallow depth of burial, normally craters are formed at the ground zero, while for small range of depth of burial, rubble mounds are formed. For moderate depths of burial, surface collapse and subsidence craters are formed and for deeply buried sources, nearly no visible surface effects have been reported due to localized chimney growth that is confined near the cavity. All these surface shapes depend on the site-specific rock mass properties, existing heterogeneities due to multiple rock formations, residual stresses due to overburden and presence of cracks, discontinuities, joints, faults and slip planes in the rock mass. Normally, there always exists some degree of uncertainty in the numerical predictions due to the above factors. Still it is possible to predict the behaviour of underground nuclear explosions through efficient computational studies.

Computer simulation of underground nuclear explosions has been used to predict and interpret experimental measurements for quite some time. First, such computations were performed for Rainier explosion by Johnson *et al.*[5], followed by Salmon experiment by Patterson[6]. Inelastic phenomena due to such explosions have been studied[7,8]. Earlier development of one- and two-dimensional finite difference codes are attributed to Wilkins[9], and Maenchen and Sack[10]. Following this, improved finite difference codes, namely the one-dimensional code, SOC73 by Schatz[11,12] and its two-dimensional version, TENSOR, attributed to Burton and Schatz[13] were developed at the Lawrence Livermore Laboratory. These Lagrangian codes integrate the conservation equations of continuum mechanics to solve problems involving stress wave propagation. The equation of motion based on conservation of mass, linear and angular momentum provides a relation between the applied stress and the acceleration of each point in the coordinate system. The energy conservation equation is not used as the heat conduction does not take place in such a short duration. However, the calculations of internal plus kinetic energy are used for checking the accuracy of calculations. Finally, the applied strains obtained for discrete time intervals generate the resulting stress fields from the equation of state of the rock medium. The rock constitutive models in the codes take into account pore collapse, both ductile and brittle failure, tensile failure with crack opening and closure, and rock melt and vaporization. The above codes have the following limitations:

(a) The inelastic processes are not modelled accurately over the full range of the explosion processes in as much as the models assume that the shear stresses do not affect the volumetric response of the material.
(b) The strain-rate enhancement effects and material hardening are not accounted. Thus the time-dependent behaviour of the geological materials observed in shock-wave studies cannot be represented. Transition from ductile to brittle behaviour is also not fairly accounted.
(c) Computations can at most be done in two dimensions or with axisymmetric models, thereby foregoing the three-dimensional nature of the geological medium and the prevailing discontinuities.

The present study uses the nonlinear finite element algorithms for geometric and material nonlinearities with suitable strain measures for quadratic terms, delimitation of calculation domain using non-reflecting boundary conditions, constitutive behaviour model for deviatoric behaviour and coupling of the volumetric behaviour with material equation of state.

Transient three-dimensional finite element code, SHOCK-3D

The three-dimensional transient code, SHOCK-3D, used in the present study is based on the coupled finite element formulation for geological medium and fluid medium to represent the different rock formations and the gas cavity near the source respectively. SHOCK-3D is an explicit, transient, three-dimensional Lagrangian finite element code for shock-wave propagation problems. This code adopts the models due to Cherry and Petersen[7], Schatz[11] and Burton and Schatz[13] for underground explosion simulation. It couples strain rate-dependent elasto-viscoplastic formulation for the geological medium with Hugoniot equation of state, and the hydrodynamic formulation for the gas medium with an equation of state in a coupled framework. For optimum computational efficiency and accuracy, eight-node isoparametric brick elements with central point integration rule and appropriate viscous dissipation are used for both the domains. The set of transient semi-discrete equations (eq. ((1)), resulting from finite element discretization is solved with explicit time integration scheme for both the domains as described below.

$$Ma^{t} + Cv^{t} + S^{t}(d(t)) = F^{t}, \tag{1}$$

where M is the diagonal mass matrix, C is the damping matrix and $S^{t}(d(t))$ and F^{t} are the internal and external force vectors respectively. The vectors a^{t}, v^{t} and d^{t} denote the acceleration, velocity and displacement vectors respectively, at time t (denoted in the superscript). The central difference time-marching scheme with time step Δt is used to integrate the above set of equations as shown in eqs (2–4).

The acceleration field $a^{t+\Delta t}$ is obtained as

$$a^{t+\Delta t} = a^{t} = M^{-1}[F^{t} - Cv^{t} - S^{t}(d(t))]. \tag{2}$$

Further, the velocity field $v^{t+\Delta t}$ is obtained as

$$v^{t+\Delta t} = v^{t} + a^{t+\Delta t}\Delta t. \tag{3}$$

The displacement field is finally obtained as

$$d^{t+\Delta t} = d^{t} + v^{t+\Delta t}\Delta t. \tag{4}$$

The internal force vector $S^{t}(d(t))$ is obtained from the internal stress field σ over the model domain Ω as

$$S^{t+\Delta t} = \int_{\Omega} B^{T}\sigma^{t+\Delta t}d'\Omega. \tag{5}$$

The displacement and velocity fields updated by eqs (3 and 4) are used to obtain the stress and strain rates at the numerical integration Gauss points. Finally the internal stress field is incremented at each time step depending on the stress rate. It is correlated with the Jaumann stress rate, which in turn is strain-rate dependent. The damping matrix C is generated with Sommerfeld[14] radiation condition to simulate a radiation boundary to avoid any spurious reflections from the model boundary with normal and tangential directions as n and t respectively, as follows.

$$\sigma_{n} = \rho c_{b} v_{n}, \tag{6}$$

$$\sigma_{t} = \rho c_{s} v_{t}. \tag{7}$$

Here σ_{n} and σ_{t} are normal and tangential stresses, v_{n} and v_{t} are the normal and tangential components of the particle velocity at the mesh boundary, ρ is the medium density and c_{b} and c_{s} are the body wave and shear wave velocities for the medium. These conditions are applied sufficiently away from the source, where plane elastic-wave condition exists.

Fluid constitutive model for gas cavity

In the gas cavity, non-viscous hydrodynamic formulation-based fluid finite elements with limited overburden pressure are used to correlate the pressure (p) with volumetric strain (ε_{v}) and specific energy E. A general form of this equation for the cavity gas is given as,

$$p = a_{1} + a_{2}(\varepsilon_{v}) + a_{3}(\varepsilon_{v})^{2} + a_{4}(\varepsilon_{v})^{3} + [a_{5} + a_{6}(\varepsilon_{v}) + a_{7}(\varepsilon_{v})^{2}]E. \tag{8}$$

Equation (8) is used to input p as a polynomial function depending on the volumetric strain level. Thus the ideal gas model, iron gas model as given by Butkovich[15,16] or any

other suitable experimental model can be obtained from eq. (8).

Solid constitutive model for the geological medium

The constitutive model due to Hoek and Brown[17] for the rock strata is available in the present code. This model accounts for the confinement effect on rock strength. Damage mechanics-based failure models are used depending on the strain levels for brittle and ductile failures. The damage mechanics failure rules are strain-based and suitable for crack profile mapping near the source. The Hugoniot equation of state at high shock pressures (in M-bar range) and hydrostatic data (in K-bar range) for shale and sandstone available for reported simulation studies similar to Butkovich[16] and Burton *et al.*[18] have been used in the present study. It may be noted that loading and unloading bulk moduli in the different regimes such as the mean pressures corresponding to the maximum tensile and compressive stresses of the rock medium at zero confinement describing the Hugoniot elastic limits, hydrostatic pressure range and high-pressure shock range are suitably included. The loading and unloading bulk moduli at different pressures are evaluated for dry rock medium. It is assumed that in the loading stage, the pores in the rock are filled up depending on the surrounding confinement generated due to pressure shock. In the unloading stage the volumetric strain corresponds to the ideal grain density, or it is between the ideal grain density and the bulk density, depending on the confinement level at the onset of unloading. This has been verified and confirmed by underground explosion simulation studies, as reported by Butkovich[16]. It has been observed that the data are important for obtaining the correct energy distribution in the rock medium, and improved computation is possible if site-specific data are available for a range of pressure values. The equation of state for the rock medium is given as,

$$p = K(\varepsilon_v) + \Gamma(\varepsilon_v)E, \tag{9}$$

where p is the hydrodynamic pressure, the local modulus $K(\varepsilon_v)$ is obtained from Hugoniot equation of state depending on the loading or unloading condition, ε_v is the volumetric strain, E is the specific energy and Γ is the Gruneisen parameter which allows dissipation of energy and is a function of volumetric strain.

Gravity effects for mound fall-back

SHOCK-3D has a provision to link the geological model with the gravity option, as described by Burton *et al.*[18], after initiation of the transient event of energy deposition. This helps to simulate the fall-back of the rising mound and spallation-induced seismic signals are also computed. The gravity load is applied as a body force term in F^t of eq. (1) and the *in situ* stresses can also be accounted with this approach. It is established through the present computations that the spall mechanism at the shale–sandstone interface due to the rarefaction wave induced the slap-down and the resultant second peak in the vertical acceleration signal in case of Pokhran-1974 nuclear explosion event[19].

Mathematical model for Pokhran-1974 event

Figure 1 shows the three-dimensional finite element model used in the present study. This model represents the three-layered geological system of shale, sandstone and degraded sandstone. In Figure 1, an enlarged view of the fluid element representing the emplacement cavity located at a

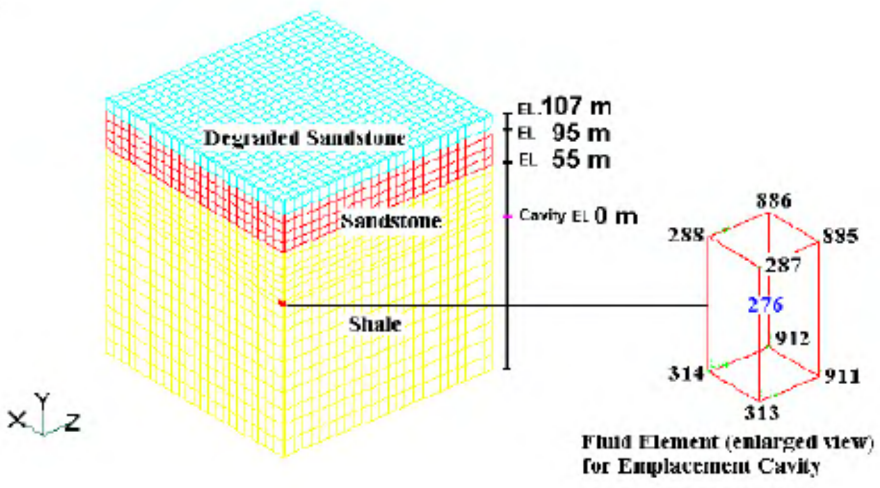

Figure 1. Three-dimensional finite element model of three-layered geological model for near source simulation. Fluid element (element number 276) used as emplacement cavity is shown in enlarged view with node numbers (black font) and element number (blue font).

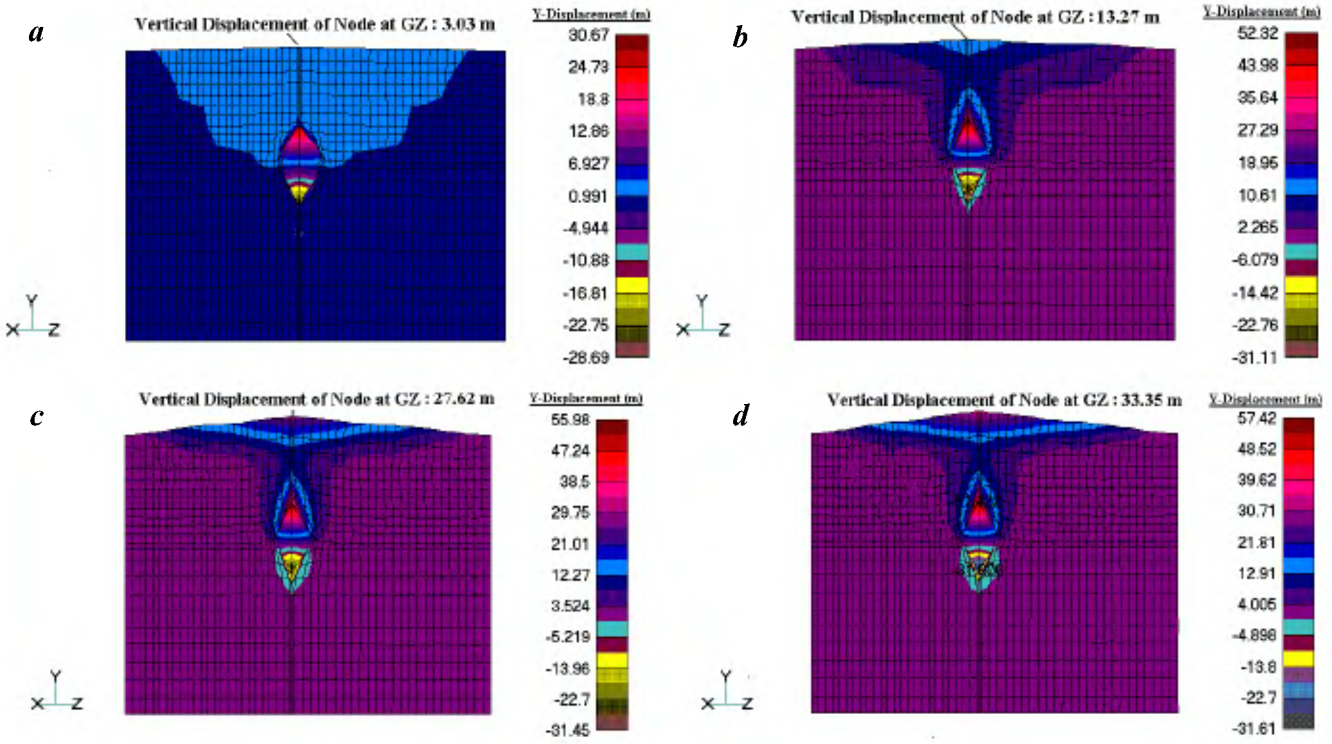

Figure 2. Cavity growth and free surface uplift (m) at (*a*) 250 ms (*b*) 1 s. (*c*) 2 s (*d*) 2.5 s.

Table 1. Properties of rock medium

Geological property	Shale	Sandstone
Density (kg/m^3)	2450	2100
Ideal grain density (kg/m^3)	2784	2800
Young modulus (MPa)	7848	4905
Poisson ratio	0.10	0.28
Unconfined compressive strength (MPa)	53.71	23.71
Unconfined tensile strength (MPa)	3.040	1.925

depth of 107 m from the top is also shown. Above this cavity, the shale stratum is up to an elevation of 55 m, which is overlaid with a sandstone cover of 40 m thickness, extending up to an elevation of 95 m. The topmost layer above this is a degraded sandstone stratum of 12 m thickness. The cubical cavity is equivalent to a spherical source with a radius of 4.18 m, where three-dimensional fluid elements are used to simulate the ionized gas medium. It is assumed that this cavity is immediately formed due to rapid vaporization and the cavity filled with vapour behaves like an ideal mono-atomic gas. This is a realistic assumption, as the ionized medium with electrons and nuclei of different rock constituents (Si, H, O, etc.) is reported to behave like an ideal mono-atomic gas, as reported by Butkovich[15]. In the vapour cavity a total energy of 12 kilo tons is deposited and it is allowed to grow in the surrounding rock medium. The sandstone and shale properties used in the present computations are listed in Table 1. Non-reflecting radiation boundary conditions are applied at a distance of 251 m from the source and symmetry conditions are applied on the two planes (x–y and y–z planes) of Figure 1 near the source. The top surface at zero ground is taken as a free surface, which reflects the compression waves.

Computational results

The present computational results are presented for short time and long time-transient phenomena to show the cavity growth, velocity and displacement profile of the cavity, top mound growth and crater formation due to subsidence. The short timescale for computation was selected to evaluate the spherically symmetric growth of the gas cavity up to an asymptotic level, displacement and velocity profiles of the cavity boundary and initial mound growth. The long-time transient computations were carried out to pick up the maximum mound growth, maximum mound velocity, oblong growth of the cavity producing chimney effect due to rarefaction wave and the resulting spallation of the rock layers. Moreover, close in-ground acceleration signals were also computed to benchmark the code predictions with the measured acceleration signals near the source with help of the short-time transient computation. These measured values are in the elastic region (135 m) from the zero ground.

Cavity growth, mound formation and cratering

Figures 2–5 show the cavity growth and mound formation obtained from the present computation up to 3.0 s duration.

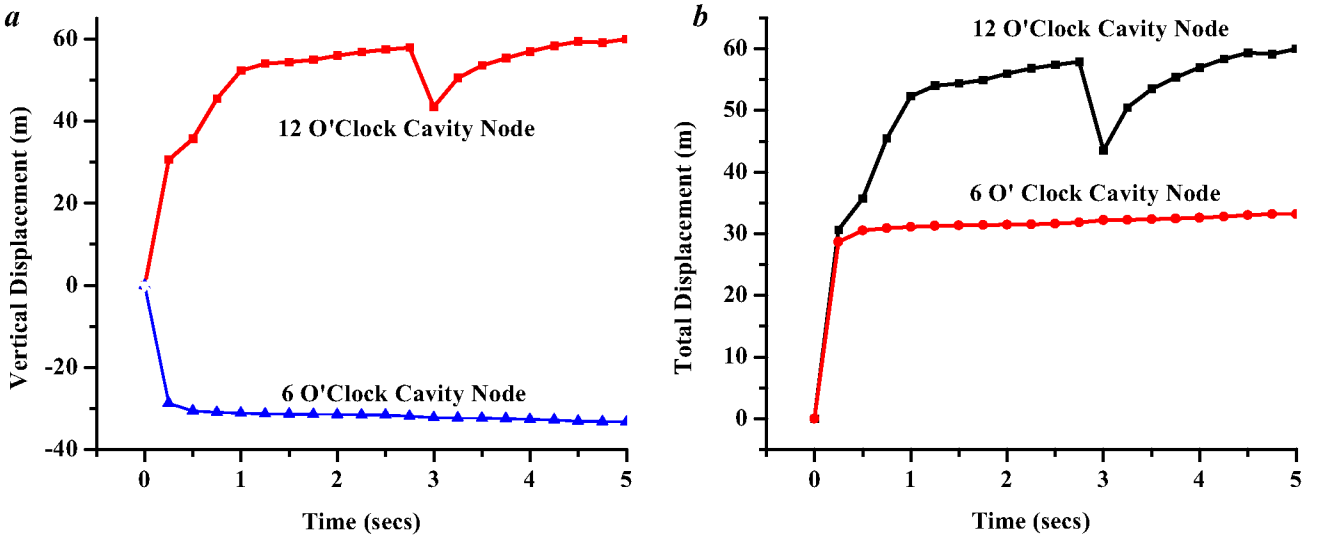

Figure 3. Plot of vertical displacement (***a***) and resultant displacement (***b***) of 12 O'clock and 6 O'clock cavity nodes (nodes 287 and 313 respectively, of cavity fluid element indicated in Figure 1).

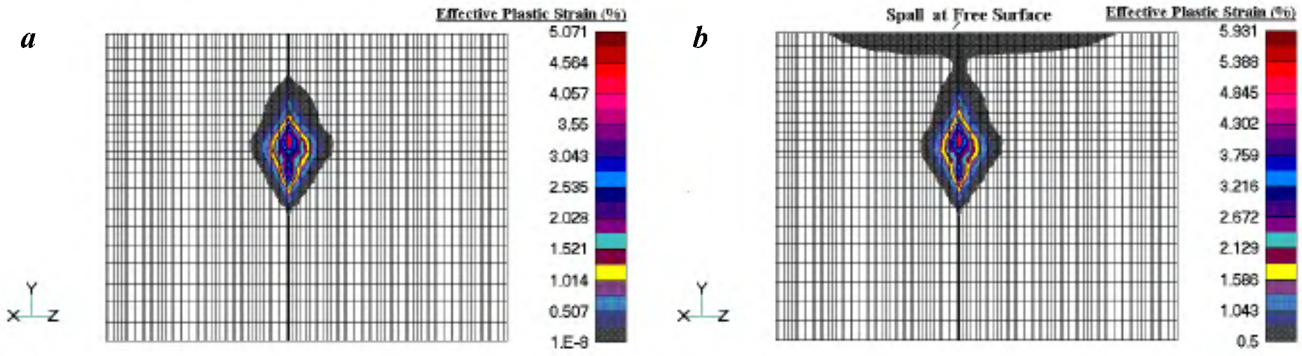

Figure 4. ***a***, Inelastic strain contours developed due to crushing and cracking around the source and cavity oblonging after 1 s. ***b***, Inelastic strain contours developed around the source due to crushing and cracking of rock layers and spall at free surface after 2 s.

The cavity instantly grows to a size of ~30 m up to 250 ms, as shown in Figure 2 *a*. Till this time the mound growth is limited to a maximum vertical displacement of 3.03 m for the node at GZ. At 1 s, significant oblonging of the cavity is observed and maximum vertical displacement for node at GZ is 13.27 m, as shown in vertical deformation contours in Figure 2 *b*. With time, the vertical mound growth increases to 27.62 m at 2 s and 33.35 m at 2.5 s, as illustrated in Figure 2 *c* and 2 *d* respectively. The cavity growth, its oblonging due to rarefaction wave reflected from GZ and mound growth are also demonstrated in the Figure 3 *a* and 3 *b*. The vertical displacement for 12 O'clock and 6 O'clock cavity nodes demonstrates that the cavity grows in an oblong manner up to 5 s. It can be noted from Figure 3 *a* that the 6 O'clock position node of the cavity grows asymptotically to a constant size of ~30 m. These cavity nodes show an asymptotic cavity growth in the range of 25–30 m, which is again consistent with the experimental value of 30 m. However, the 12 O'clock position node shows monotonic oblonging up to 2.5 s, which is consistent with the mound growth period of similar order. The influence of mound fall-back on the cavity deformation is observed with a dip in deformation value. Subsequently, during the gas acceleration phase, the 12 O'clock position node of the cavity further moves up to a constant value of ~60 m. Similar observation is noted in the plot of absolute scalar value of cavity node deformation presented in Figure 3 *b*. Figure 4 *a* shows the inelastic strain contours developed around the source at 1 s due to crushing and cracking of the rock. The maximum effective plastic strain at this time is of ~5.07%, observed very near to the source. Figure 4 *b* shows the inelastic strain contours developed in the rock medium at 2 s due to free surface spall. The peak strain levels are confined near the cavity and the strain levels at the free surface are of lower order. This behaviour is due to the typical hard-rock medium that resulted in zero venting with full confinement of the event, as reported by Chidambaram *et al.*[1,2]. The computed inelastic strain profile is shown in Figure 4 *b*, and it is demonstrated that the

inelastic zone extends up to a distance of ~100 m from the GZ. This is consistent with the observed value of the inelastic zone of 80–114 m noticed during post-shot examination after the event, as reported by Chidambaram *et al.*[1,2].

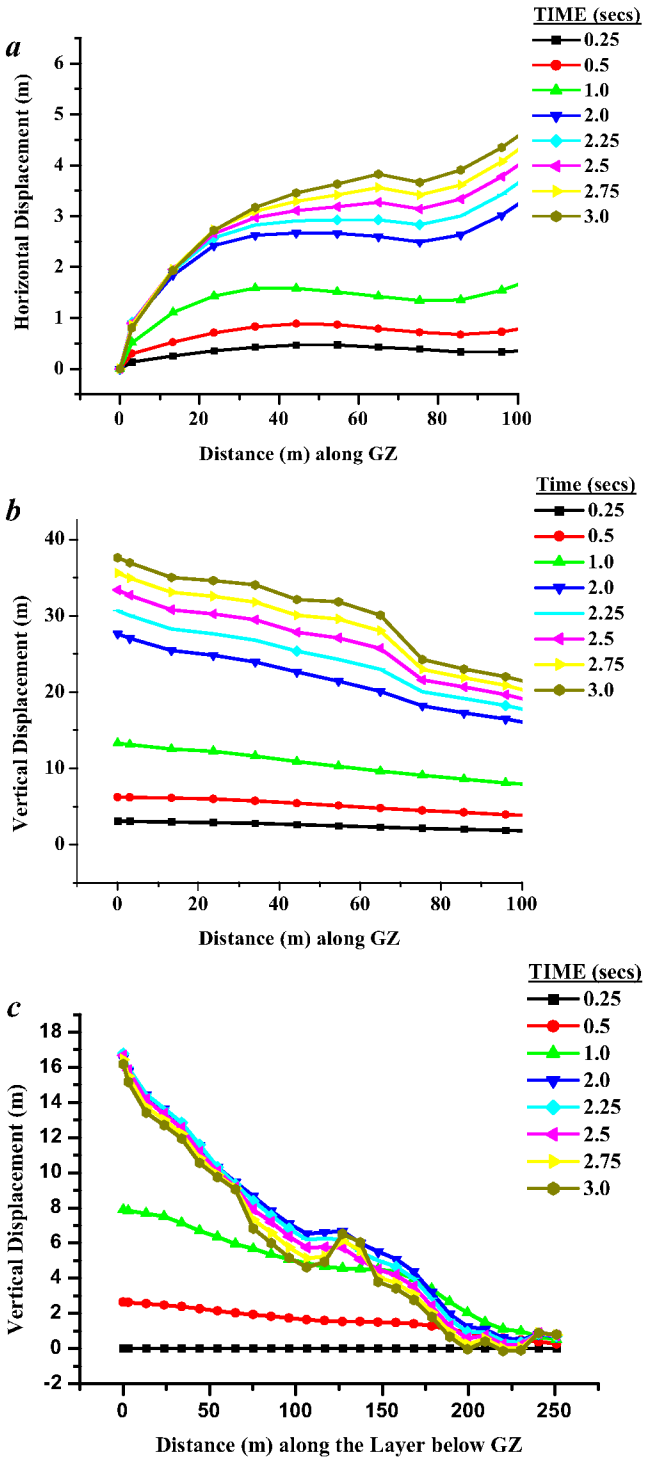

Figure 5. Time history of horizontal displacement (*a*) and vertical displacement (*b*) nodes along free surface at GZ (up to a distance of 100 m). (*c*) Time history of vertical displacement of nodes along a layer below GZ (up to a distance of 100 m).

Mound growth phenomenon is also presented in Figures 5 *a* and *b*, which gives the horizontal and vertical deformation time histories up to 3 s for nodes along the free surface, starting from the node at GZ and extending up to a distance of 100 m. Here also, it can be seen that the computed value of mound uplift is in the range of ~33.35 m at 2.5 s to ~37 m at 3 s, which is in close agreement with the earlier reported value of mound uplift of ~34 m (refs 1, 2) at the test site. Also, the horizontal displacement increases with distance from GZ node and reaches its maximum at radial distances in the range of 80–85 m. This extent of radial growth identifies the observed mound radius of 85 m. Figure 5 *c* demonstrates spalling at the free surface and splitting at the interface/sublayer below GZ in the present computations. The plot shows the vertical displacement histories up to 3 s for a layer below GZ. Here it can be observed that at a radial distance ~85 m from the GZ the vertical growth nearly ceases, whereas the upper layer continues to rise as seen in Figure 5 *a*. Thus, a zone extending radially up to distance of ~85 m from the GZ is the influence zone, where cracking is predominant.

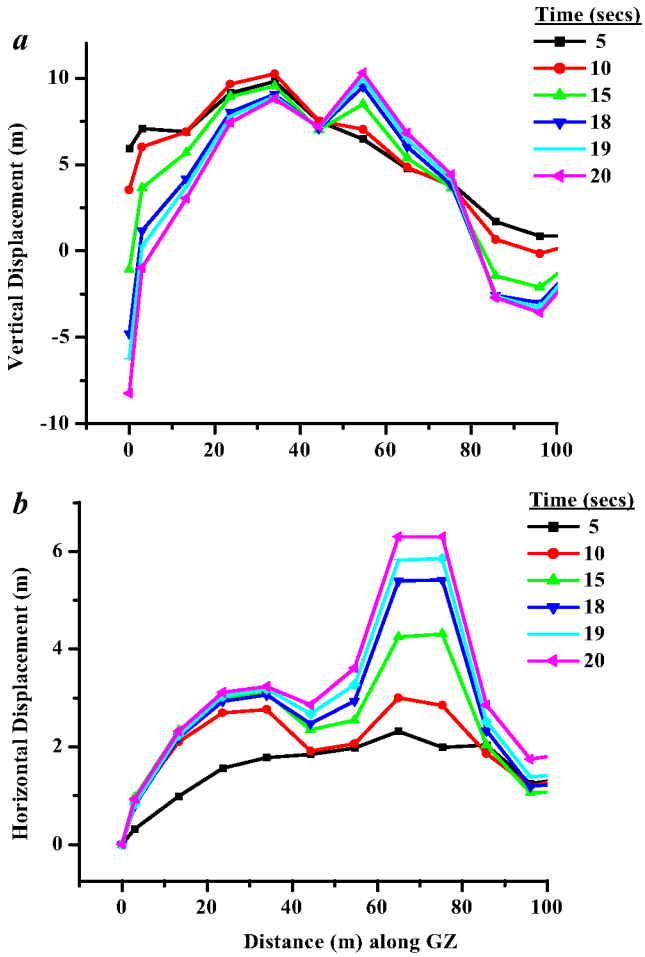

Figure 6. Time history of vertical displacement (*a*) and horizontal displacement (*b*) of nodes along free surface at GZ (up to a distance of 100 m).

Crater formation due to mound fall-back is presented in Figure 6 *a* and *b*. Vertical fall-back has been computed starting at 5 s and extending up to 20 s as seen in Figure 6 *a*. The fall-back is nearly complete after 6–7 s, where the computed vertical deformation is in the range of 5–7 m. Further settlement takes place after a longer time and the final observed crater depth is 9 m at 20 s. The crater radius can be identified from Figure 6 *a*, where the fall-back zone is 40–47 m in radius. These computations are in excellent agreement with the observed crater depth of 10 m and crater radius of 47 m. Figure 6 *b* gives the horizontal deformation time histories up to 20 s for nodes along the free surface. Here, it can be observed that the maximum horizontal extension takes place at a radial distance range of 45–65 m beyond which horizontal deformation is insignificant. This horizontal movement is responsible for the subsidence zone and the surrounding crater lip that has been observed after the event.

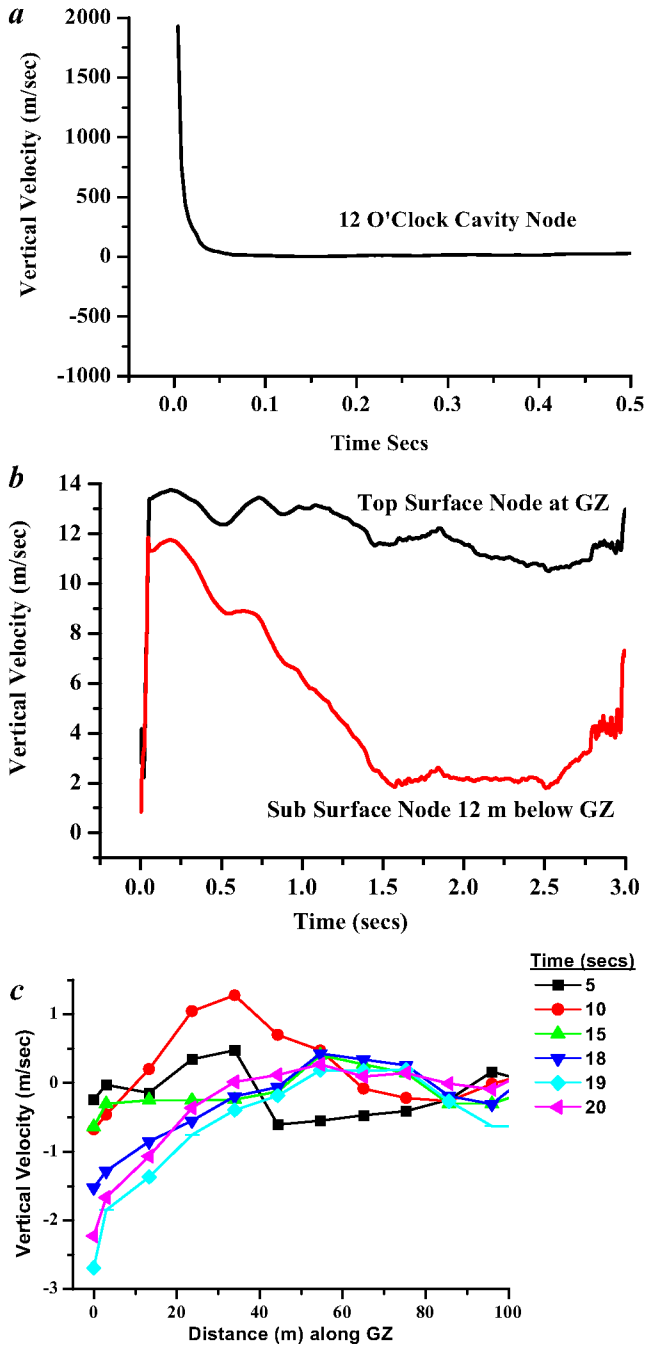

Figure 7. ***a***, Time history of vertical velocity (m/s) of 12 O'clock cavity node up to 0.5 s. ***b***, Time history of vertical velocity (m/s) of free surface node at GZ and node 12 m below GZ up to 3 s. ***c***, Time history of vertical velocity (m/s) of nodes along free surface at GZ (up to a distance of 100 m).

The velocity of the top cavity node has been plotted up to 3 s in Figure 7 *a*. The initial peak value of 1000 m/s of the vertical velocity is in confirmation with the earlier reported value in the range ~1000 m/s at 5 ms. The vertical velocity profiles up to 3 s for nodes along the free surface at GZ and for the shale–sandstone interface, identified here by a layer 12 m below the free surface, are presented in Figure 7 *b*. The computed peak vertical velocity at GZ node is 16 m/s and for the node below GZ it reduces to ~12 m/s. Differential velocity pattern of these two layers can be observed in the plots, which show the separation of layers in this 12 m depth zone. Figure 7 *c* presents the time histories of vertical velocity of nodes along the free surface at GZ up to a distance of 100 m. Here it can be seen that at times after 6–7 s, the top surface has nearly come to rest and only a zone of radius 40–47 m shows an asymptotic downward movement leading towards the final crater formation.

Comparison of synthetic seismic signals with measured signals

Figure 8 *a* and *b* shows the vertical acceleration up to 3 s for nodes located at the free surface sensor positions of ~137 and ~147 m from the GZ. In this case, the gravity link of the computation has been activated after 0.5 s of the event, which takes a finite computational time to simulate the quasi-static initial stress field due to the gravity in the transient analysis. The initial peak of 90–105 m/s^2 in the vertical acceleration recorded at 135 m from the zero ground is shown (Figure 8). Subsequently, a peak vertical acceleration of 115–120 m/s^2 is observed after 2.25 to 2.75 s of the event, which was actually observed in the real time of 2.0 to 2.5 s after the event in the geophone records at 4 and 6 km range, and also in teleseismic spectra at Hagfors (Sweden), Stollet (Sweden) and Yellowknife Array (Canada), as reported in Chidambaram *et al.*[1]. The small lag of ~0.25 s in the second peak of the computed acceleration compared to the recorded signal is due to the gravity link time of 0.5 s used for the computation, as the initial stress effects are simulated in a quasi-static manner with a finite computational time, till the influence of the gravity field is stabilized. The second peak is due to the slap-down of the spalled rock layer of 60 m near the shale–sandstone interface, as reported by Chidambaram *et al.*[1] and has also been sensed

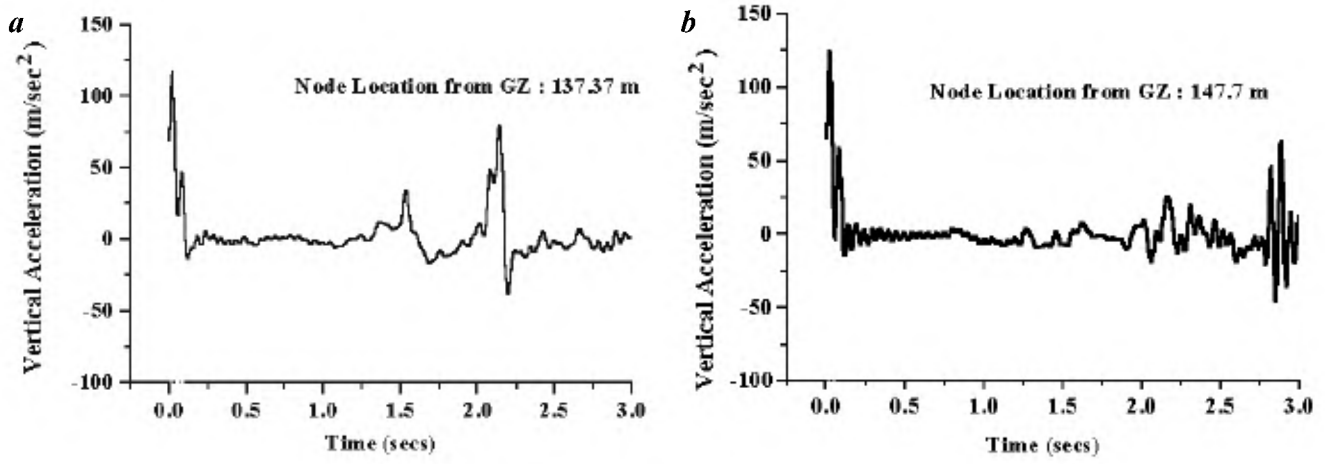

Figure 8. Time history of vertical acceleration (m/s^2) of free surface node at (***a***) 137.37 and (***b***) 147.7 m from GZ.

at the above teleseismic stations. The initial acceleration peak, the second vertical acceleration peak due to slap-down and the acceleration–time signal profile are in excellent agreement with the recorded values. This confirms that in Pokhran-1974 event, the principal mechanism for the observed second acceleration peak was spall-induced slap-down.

Conclusions

The present study gives an overall view of the nuclear explosion simulation for the Pokhran-1974 event on a global three-dimensional model with finite element code, SHOCK-3D. The peak particle velocity at the zero ground, cavity size and oblong growth of the cavity (chimney effect) due to the rarefaction waves, mound growth, its fall-back and final crater dimensions have been successfully computed and are consistent with the recorded values. The failure mechanism due to spall and crushing is also shown to be consistent with the test values. SHOCK-3D is also capable of generating the synthetic seismic signals at the elastic radius and has been found to have good comparison with the close in-ground recorded values.

1. Chidambaram, R. and Ramanna, R., Some studies on India's peaceful nuclear explosion experiment. IAEA-TC-I-4/19, 1975, pp. 421–436.
2. Chidambaram, R., Sikka, S. K. and Gupta, S. C., Phenomenology of the Pokhran PNE experiment. *Pramana*, 1985, **24**, 245–258.
3. Rodean, R. C., Inelastic processes in seismic wave generation by underground explosions. In *Identification of Seismic Sources–Earthquake or Underground Explosion* (eds Husehye, E. S. and Mykkoltveit, S.), Proc. NATO, ASI, Oslo, Norway, 8–18 September 1980.
4. Allen, B. M., Drellack. Jr. S. L. and Townsend, M. J., *Surface Effects of Underground Nuclear Explosions*, Bechtel, Nevada, 1997.
5. Johnson, G. W., Higgins, G. and Violet, C., Underground nuclear detonations. *J. Geophys. Res.*, 1959, **64**, 1457–1470.
6. Patterson, D. W., Nuclear decoupling, full and partial. *J Geophys. Res.*, 1966, **71**, 3427–3436.
7. Cherry, J. T. and Petersen, F. L., Numerical simulation of stress wave propagation from underground nuclear explosions. In *Peaceful Nuclear Explosions*, IAEA-PL-388/15, IAEA, Vienna, 1970, pp. 241–325.
8. Terhune, R. W., Glenn, H. D., Burton, D. E. and Rambo, J. T., Containment analysis for the simultaneous detonation of two nuclear explosions, Lawrence Livermore Laboratory, Report UCRL-52268, Livermore, California, 1977.
9. Wilkins, M. L., Calculation of elastic–plastic flow. In *Methods in Computational Physics*, Academic Press, New York, 1964, vol. 3.
10. Maenchen, G. and Sack, S., The tensor code. *Methods in Computational Physics*, Academic Press, New York, 1964, vol. 3.
11. Schatz, J. F., The physics of SOC and TENSOR code. UCRL-51352, 21 February 1973.
12. Schatz, J. F., SOC73, A one-dimensional wave propagation code for rock media. Lawrence Livermore Laboratory, Report UCID-51689, Livermore, California, 1974.
13. Burton, D. E. and Schatz, J. F., Rock modelling in TENSOR'74, a two-dimensional Lagrangian shock propagation code, Lawrence Livermore Laboratory, Report UCID-16719, Livermore, California, 1975.
14. Sommerfeld, A., *Partial Differential Equations in Physics*, Academic Press, 1949.
15. Butkovich, T. R., Gas equation of state for natural materials, UCRL-14729, 24 January 1967.
16. Butkovich, T. R., Techniques for generating pressure–volume relationships and failure envelopes for rocks, UCRL-51441, 1 November 1973.
17. Hoek, E. and Brown, E. T., Practical estimates of rock mass strength. *Int. J. Rock Mech. Min. Sci.*, 1998, **34**, 1165–1186.
18. Burton, D. E., Snell, C. M. and Bryan, J. B., Computer design of high-explosive experiments to simulate subsurface nuclear detonations. *Nucl. Tech.*, 1975, **26**, 65–87.
19. Ranjan, Rajeev, Singh, R. K., Sikka, S. K. and Kakodkar, A., Three-dimensional Finite Element Simulation of PNE Events [rev 01]: Restricted report for internal communication, October 1999.

Received 15 June 2004; revised accepted 17 November 2004

Antenna beam tilting effects in fixed and mobile communication links

M. V. S. N. Prasad*, M. M. Gupta, S. K. Sarkar and Iqbal Ahmad

Radio and Atmospheric Sciences Division, National Physical Laboratory, Dr K. S. Krishnan Road, New Delhi 110 012, India

Several remedial measures like space diversity, frequency diversity, route diversity, increase in antenna height, antenna tilting, etc. have been tried by many workers to overcome the debilitating effect of multipath fading in fixed line-of-sight microwave and mobile communication links. Among these remedial measures, diversity techniques have been extensively studied in terms of improvement factor, whereas the concept of antenna tilting is relatively less explored compared with other remedial measures. In the present study, the effect of antenna tilting on fixed and mobile communication links is investigated to find out the optimum tilting angles in terms of design parameters.

ANTENNA beam tilting effects have been effectively employed in the past to overcome multipath fading induced by super-refractive/ducting layers in microwave fixed line-of-sight (LOS) links. These approaches and experiments helped to design angle diversity schemes in LOS links. In these cases, upward tilting of the antenna cuts-off or reduces the radio frequency energy refracted by the ground-based layers and reduces the multipath fading[1,2]. Taking the clue from these experiments, some workers have tried to employ the concept of tilting on mobile communications in cellular networks. It has been observed that downward tilting of antenna beam can reduce the interference effects in other macro cells. Since super-refractive and ducting layers would not affect the performance of cellular networks, upward tilting of antenna beam cannot yield appreciable improvements, except in special situations. Downward tilting decreases the probability of occurrence of unacceptable inter symbol interference (ISI) due to multipath propagation by diminishing the power level of echoes with long delay times. Delay time determines the rms delay spread, which in turn determines the transmissible bit rate. In analogue systems, fade depth can be decreased. In mobile communications, when the cell site uses a high gain antenna, downward tilting can direct the nulls in the antenna pattern towards the horizon to prevent the energy from propagating into other cells.

Advantages of downward tilting

When the cell site uses a high-gain antenna, downward tilting can direct the nulls in the antenna pattern towards the horizon to prevent energy from propagating into other cells. In the case of a low-gain antenna, discrimination between horizon and edge of a cell is less. This can be improved with increase in height. Using a high gain, high antenna elevation and downward tilting, the base-station can reduce its power relative to what would be required from a low-elevation site. When the antenna height is close to that of buildings, any height increase would degrade the delay spread due to long-distance reflectors. It seems that high sites and downward tilting cannot be effectively used without each other[3]. Improvement in raising base-station antenna is offset by long-distance reflectors, if downward tilting is not used. Also, in the case of a low-site, downward tilting is ineffective because the edge of a cell cannot be discriminated from the horizon. High antenna with downward tilting will be able to discriminate the edge of the intended coverage area and significantly reduce system interference. Upward tilting is useful if radio energy has to be reached in the upper floors of high-rising towers. Figure 1 illustrates the basic concept of antenna tilting. Chang and Kim[4] have shown that a tilting angle of 10° is necessary to obtain the effectiveness of down-tilt. Blackard *et al.*[5] observed decrease in path loss and increase in delay spread with antenna height. Effect of low antennas with tall buildings on either side was reported[6,7]. DeWeck *et al.*[8] studied delay spread in mountainous terrain using various antenna patterns and heights. To avoid potential reflectors, they recommended high-gain antennas with appropriate down-tilting. Low antenna heights (13, 3 m) were studied by Feurestein *et al.*[9] without tilting.

Results

In the present study an attempt has been made to find out the effects of tilting by evaluating system performance under multipath distortion. In the fixed category, effects of upward

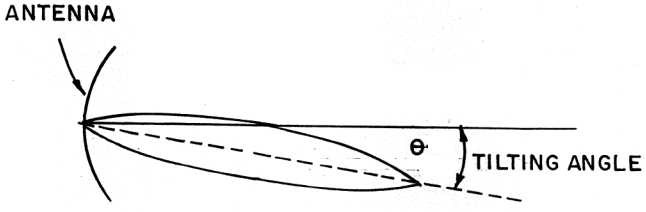

Figure 1. Illustration of the concept of antenna tilting.

*For correspondence. (e-mail: mvprasad@mail.nplindia.ernet.in)